PNAS Nexus, 2023, 2, 1–10
https://doi.org/10.1093/pnasnexus/pgad108
Advance access publication 29 March 2023
Research Report

Rare-earth control of phase transitions in infinite-layer nickelates

Yajun Zhang[a,b,*,1], Jingtong Zhang[c,d,e,1], Xu He[c], Jie Wang[d,e] and Philippe Ghosez[c]

[a]Key Laboratory of Mechanics on Disaster and Environment in Western China Attached to The Ministry of Education of China, Lanzhou University, Lanzhou 730000 Gansu, China
[b]Department of Mechanics and Engineering Science, College of Civil Engineering and Mechanics, Lanzhou University, Lanzhou 730000 Gansu, China
[c]Theoretical Materials Physics, Q-MAT, CESAM, Université de Liège, B-4000 Liège, Belgium
[d]Department of Engineering Mechanics and Key Laboratory of Soft Machines and Smart Devices of Zhejiang Province, Zhejiang University, 38 Zheda Road, Hangzhou 310027, China
[e]Zhejiang Laboratory, Hangzhou, 311100 Zhejiang, China
*To whom correspondence should be addressed. Email: zhangyajun@lzu.edu.cn
[1]Y.Z. and J.Z. contribute equally to this work.
Edited By: Vicki Grassian

Abstract

Perovskite nickelates $RNiO_3$ (R = rare-earth ion) exhibit complex rare-earth ion dependent phase diagram and high tunability of various appealing properties. Here, combining first- and finite-temperature second-principles calculations, we explicitly demonstrate that the superior merits of the interplay among lattice, electron, and spin degrees of freedom can be passed to $RNiO_2$, which recently gained significant interest as superconductors. We unveil that decreasing the rare-earth size directly modulates the structural, electronic, and magnetic properties and naturally groups infinite-layer nickelates into two categories in terms of the Fermi surface and magnetic dimensionality: compounds with large rare-earth sizes (La, Pr) closely resemble the key properties of $CaCuO_2$, showing quasi-two-dimensional (2D) antiferromagnetic (AFM) correlations and strongly localized $d_{x^2-y^2}$ orbitals around the Fermi level; the compounds with small rare-earth sizes (Nd–Lu) are highly analogous to ferropnictides, showing three-dimensional (3D) magnetic dimensionality and strong k_z dispersion of $d_{3z^2-r^2}$ electrons at the Fermi level. Additionally, we highlight that $RNiO_2$ with R = Nd–Lu exhibit on cooling a structural transition with the appearance of oxygen rotation motion, which is softened by the reduction of rare-earth size and enhanced by spin-rotation couplings. The rare-earth control of k_z dispersion and structural phase transition might be the key factors differentiating the distinct upper critical field and resistivity in different compounds. The established original phase diagram summarizing the temperature and rare-earth controlled structural, electronic, and magnetic transitions in $RNiO_2$ compounds provides rich structural and chemical flexibility to tailor the superconducting property.

Keywords: infinite-layer nickelates, rare-earth control, magnetic dimensionality, phase transitions, phase diagram

Significance Statement:

The discovery of superconductivity in $RNiO_2$ infinite-layer nickelate compounds has recently generated a huge interest. Strikingly, the fundamental physics are strongly rare-earth dependent. Here, a general lattice–electron–spin relationship is established through first- and second-principles techniques. We unveil that reducing rare-earth size softens in-plane rotation, controls the crystal field splitting, and tunes the competition between strongly localized Ni $d_{x^2-y^2}$ bands and itinerant Ni $d_{3z^2-r^2}$ bands, which divides infinite-layer nickelates into two groups with distinct Fermi surface, k_z dispersion, and magnetic dimensionality. We further bridges different communities by making an explicit comparison with high-T_c cuprate and iron superconductor. A complete temperature-dependent phase diagram of this emergent family of compounds and an unified discussion of their structural, electronic, and magnetic properties are achieved.

Infinite-layer nickelates $RNiO_2$ (R = rare-earth ion) attracted increased interest since the recent discovery of superconductivity (1, 2). The observation of superconductivity in this family of d^9 compounds provides indeed an exciting new platform to explore the physics of high-T_c superconductors and has boosted numerous theoretical and experimental studies (1–43).

Comparing with the $RNiO_3$ perovskites, $RNiO_2$ can be viewed as derivatives with the removal of the apical oxygen atoms. In $RNiO_3$, due to the complex interplay among charge, orbital, spin, and lattice degrees of freedom, compounds with different rare-earth ion exhibit quite distinct behaviors and properties (44, 45). As r_R decreases, the antiferrodistortive (AFD) rotation pattern changes from $a^-a^-a^-$ to $a^-a^-c^+$ from La to Pr–Lu, and the rotation amplitudes notably increase. The magnetic order undergoes paramagnetic (PM) to antiferromagnetic (AFM) transition, and the Néel temperature first increases and then decreases continuously

Competing Interest: The authors declare no competing interest.
Received: October 5, 2022. **Accepted:** March 16, 2023

with decreasing r_R. In terms of electronic properties, with the decrease of r_R, the bond disproportionation becomes stronger and there is a transition from the metallic to insulating phase and the band gap increases smoothly (44, 45).

Interestingly, in the $RNiO_2$ family, depending on the R-site ion, there is also a large diversity of their properties. For example, the magnitude and anisotropy of the superconducting upper critical magnetic field (H_{c2}) in $LaNiO_2$, $PrNiO_2$, and $NdNiO_2$ are strikingly different. $LaNiO_2$ and $PrNiO_2$ exhibit strong anisotropy of the upper critical field similar with that of cuprates (39). However, an unexpected isotropy of H_{c2} is observed in $NdNiO_2$ (5, 6, 39). This behavior is at odds with that of cuprates, but analogous to that of ferropnictides. In the latter, the isotropic H_{c2} has been related to the k_z dispersion of bands at the Fermi surface (46). Note that ferropnictides with three-dimensional (3D) magnetic couplings are multiband systems with both Mott-localized and itinerant electrons and exhibit a 3D Fermi surface. In contrast, Mott-insulating cuprates with two-dimensional (2D) magnetic couplings exhibit single-band character. These suggest that rare-earth control of electronic transition across the $RNiO_2$ family might be the key factor for the strong difference in H_{c2}.

On the other hand, striking difference also exists in the temperature-dependent resistivity. An unusual upturn of resistivity is observed in $NdNiO_2$ at low temperature (1), which is not obvious in $LaNiO_2$. It is known that superconducting LaOFeAs (47) and $Sr_3Rh_4Sn_{13}$ (48) also exhibit temperature-dependent resistivity anomaly, both are driven by the structural phase transition. In related $RNiO_3$ perovskites, AFD rotation of the NiO_6 octahedra typically reduces orbital hybridization and localizes electrons, resulting in enhanced resistivity, band gap, and metal-insulator transition temperature (45, 49). $NdNiO_2$ can be seen as a defective $NdNiO_3$ perovskite with missing apical oxygen atoms. Although oxygen rotation motion has never been previously reported in infinite layer $NdNiO_2$, it might be questioned if rotation of NiO_4 squares could eventually induce the anomaly of resistivity.

More broadly, investigations on $RNiO_2$ compounds primarily focused so far on the electronic and magnetic properties of the high-symmetry $P4/mmm$ phase, while lattice effects and the interplay between different degrees of freedom received much less attention. In related $RNiO_3$ perovskites, recent works highlighted the strong interplay between electronic and structural degrees of freedom (50–53). Mercy et al. (50) pointed out that the breathing distortions and metal-insulator transition are triggered by AFD oxygen rotation motions. Consistently with that, tuning of the electronic properties from the control of AFD motions has been realized in heterostructures (54). Identifying the fundamental role of R-site cation and achieving a more global description of the interplay among structural, electronic, and magnetic properties of $RNiO_2$ compounds would facilitate the full optimization of their superconducting properties.

In this work, combining first-principles calculations at zero Kelvin and second-principles calculations at finite-temperature, the interplay among lattice, electron, and spin degrees of freedom in $RNiO_2$ compounds is investigated to provide a consistent model to explore the ground state properties, reconcile different experimental observations, and hopefully disentangle the origin of different behaviors in the infinite-layer nickelates.

From lattice dynamic analysis, our calculations first reveal the presence of out-of-phase rotation motion of NiO_4 squares in $RNiO_2$ (R = Nd–Lu), reminiscent of the rotations of BX_6 octahedra in ABX_3 perovskites, where A is alkaline-earth or rare-earth element, B is transition metal element, and X (chalcogenide, oxide, and halide) is an anion. From this, the microscopic origin of the abrupt upturn of resistivity in $NdNiO_2$ is rationalized.

We further reveal that the R cation has profound impacts on the Fermi surface and magnetic dimensionality, thereby yielding $RNiO_2$ into two possible states: (i) one with marked electronic and magnetic similarities with quasi-2D AFM $CaCuO_2$ for R = La–Pr with $d_{x^2-y^2}$ bands at the Fermi surface, and (ii) another state with a striking resemblance in the magnetic dimensionality with iron superconductors for R = Nd–Lu with $d_{3z^2-r^2}$ bands occupying the Fermi energy. The direct links among geometrical effect, electronic structure, and magnetic order are established. We suggest that the R-site cation-tuned strength of the out-of-plane Ni $d_{3z^2-r^2}$ band dispersion in La (Pr)NiO_2 and $NdNiO_2$ are likely responsible for their strong difference in the anisotropy of H_{c2}. Eventually, we demonstrate that as in $RNiO_3$ perovskites, rare-earth ion controlled structural, electronic, and magnetic properties can give rise in $RNiO_2$ compounds to a rich phase diagram, which offers a unique opportunity to control desired properties by external strategy.

Results

Rare-earth ion substitution in perovskites and related compounds is well known as an efficient parameter for tuning phase transitions and has become an essential factor to differentiate the behaviors of different compounds within the same family like in $RNiO_3$ (44, 45) and the investigated $RNiO_2$ systems (1, 39). Achieving a deeper understanding of the variation of ground state properties across the $RNiO_2$ series would be a crucial step for rationalizing the exact roles of rare-earth ion.

Rare-earth control of structural transition

We start our study with a careful re-investigation of the structural properties of $RNiO_2$ compounds (R = La, Pr, Nd, Sm, Eu, Gd, Tb, Dy, Ho, Er, Tm, and Lu), relaxing first their $P4/mmm$ phase in A-AFM, C-AFM, ferromagnetic (FM), and G-AFM orders (see Fig. S1). To probe the dynamical stability of $P4/mmm$ $RNiO_2$, we then calculated the phonon dispersion curves of $LaNiO_2$, $NdNiO_2$, $TbNiO_2$, and $LuNiO_2$ in both the magnetic and nonmagnetic phases. Surprisingly, although $LaNiO_2$ appears as dynamically stable (see Fig. 1A), $NdNiO_2$, $TbNiO_2$, and $LuNiO_2$ in their AFM state all show sizable phonon instabilities as illustrated in Fig. 1B to D. Moreover, decreasing the size of the R-site cation radius when going from $NdNiO_2$ to $LuNiO_2$, the number and amplitude of the instabilities progressively increase. The dominant instability is always an A_4^- mode associated with AFD out-of-phase rotation of the NiO_4 squares around the c axis. The unstable modes in $LuNiO_2$ are shown in Fig. 2A to D. The progressive destabilization of oxygen square rotation motion as the size of the R-site cation decreases is reminiscent of what is observed for the AFD motions of the oxygen octahedra in $RNiO_3$ perovskites (50, 55) (Fig. S2). Importantly, we notice that previous calculations in the nonmagnetic state (27–29) missed the structural instability of $NdNiO_2$ (as further confirmed here in Fig. 1B), while our present calculations reveal its presence when properly deals with the magnetic character recently confirmed experimentally (4), which reflects the spin-assisted instability of rotation distortion through the strong spin-rotation coupling.

In order to identify the ground-state structure of $RNiO_2$ compounds, we fully relaxed various possible structures by condensing individual and combined phonon instabilities, taking $NdNiO_2$ and $LuNiO_2$ as prototypical examples. In both cases, the identified ground state is an $I4/mcm$ phase obtained from the condensation of the A_4^- unstable mode of the $P4/mmm$ phase.

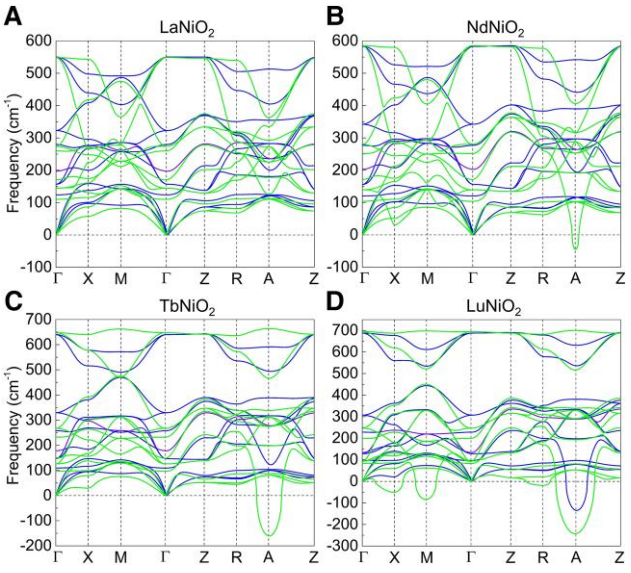

Fig. 1. Dynamical properties of $RNiO_2$ compounds. Phonon dispersion curves of A) $LaNiO_2$, B) $NdNiO_2$, C) $TbNiO_2$, and D) $LuNiO_2$ in their *P4/mmm* ground state magnetic phase and nonmagnetic phase. The blue curves and green curves represent the results from the nonmagnetic phase and magnetic phase, respectively. The high-symmetry points are denoted by: Γ = (0, 0, 0), *X* = (0, 0.5, 0), *M* = (0.5, 0.5, 0), *Z* = (0, 0, 0.5), *R* = (0, 0.5, 0.5), and *A* = (0.5, 0.5, 0.5). The unstable mode at high-symmetry A point is the out-of-phase rotation of the NiO_4 square.

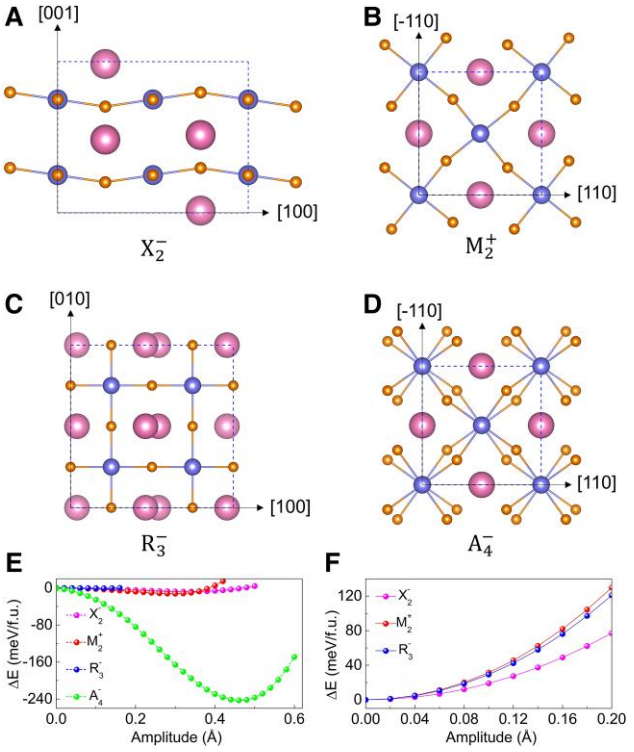

Fig. 2. Unstable modes and lattice competition. Schematic pictures of the unstable modes in $LuNiO_2$ including A) X_2^-, B) M_2^+, C) R_3^-, and D) out-of-phase rotation A_4^-. PESs of $LuNiO_2$ along the lines of atomic displacements corresponding to E) the individual unstable modes at high-symmetry points and F) the same modes but with A_4^- mode condensed with its natural amplitude into the structure.

For $NdNiO_2$, this ground state is natural since A_4^- mode is the only phonon instability. For $LuNiO_2$, the situation is more complicated as there are more unstable modes. However, the A_4^- instability remains dominant. As illustrated in Fig. 2E, the double-well potential energy surface (PES) associated with the A_4^- mode is significantly deeper than that related to other instabilities. Then, it is further clarified in Fig. 2F that, when condensing the A_4^- mode with its natural amplitude, other weaker instabilities disappear (i.e. all curves switch from double- to single-well shape). This reveals an inherent competition between out-of-phase rotation and other unstable modes: the appearance of the stronger rotation motion completely suppresses the other instabilities, stabilizing the *I4/mcm* structure as the ground state. Figure S3 shows a comparison between the energy of the possible phases in both the C-AFM and G-AFM states. It is obvious that a *P4/mmm*-*I4/mcm* structural phase transition with the appearance of $a^0a^0c^-$ rotation motion for *R* = Nd–Lu and a G-AFM-C-AFM magnetic transition occur simultaneously as the size of rare-earth ion decreases.

Unusual upturn of resistivity

Having established that $RNiO_2$ infinite-layer compounds are prone to AFD distortions, the natural question that arises concerning the temperature at which rotation appears. To access the finite-temperature behavior, we built a second-principles model (56) with the amplitudes of individual in-plane oxygen motion along the edges of NiO_4 squares as degrees of freedom in the spirit of what was done by Zhong, Vanderbilt, and Rabe for perovskites (57). The model is directly fitted on first-principles data and finite-temperature properties are accessed from Monte Carlo simulations. A detailed description of the model is provided in the Method section.

Results of the Monte Carlo simulations for $NdNiO_2$ are reported in Fig. 3A that summarizes the temperature evolution of the average displacement associated to AFD oxygen rotation. The figure clearly highlights a structural phase transition from the high-symmetry *P4/mmm* phase to the low-symmetry *I4/mcm* phase. The displacive (58) or order-disorder (59) nature of the transition can be identified by anharmonic lattice-dynamics Hamiltonian (60) and probability distribution analysis (61). It is found that the phase transition temperature T_R from the revised Perdew–Becke–Erzenhof functional for solids (PBEsol) (62) + *U* (63) with *U* = 2.5, 2.7, and 3 eV are very close to 70 K, after which the resistance begins to increase (1).

To verify whether the predicted structural phase transition is the key factor that leads to the unusual upturn of resistivity of $NdNiO_2$ observed at low temperature (1) and shed light on the actual connection between temperature and electronic structure, the band structure of high-temperature *P4/mmm* phase and low-temperature *I4/mcm* phase are compared in Fig. 3B to E. Clearly, the band structures reflect the fact that the electronic structure at the Fermi level is very sensitive to the rotation distortion, thus confirming the dramatic influence of temperature. In detail, we found that although Nd d_{xy} orbital is insensitive to temperature and rotation amplitude, the band edges of Nd $d_{3z^2-r^2}$ orbital and Ni $d_{3z^2-r^2}$ orbital at the Γ point of the band structure shift to an energy higher than the Fermi level, which significantly reduces the self-doping effect.

To quantify to which extent oxygen rotation suppressed self-doping effect can be a reliable explanation for the upturn of resistivity, a direct comparison of resistivity obtained from the Boltzmann transport equation (64) in the high-temperature *P4/mmm* phase and low-temperature *I4/mcm* phase is shown Fig. S4, it is clear that the resistivity around the Fermi level increases significantly in the low-temperature phase. Therefore, in

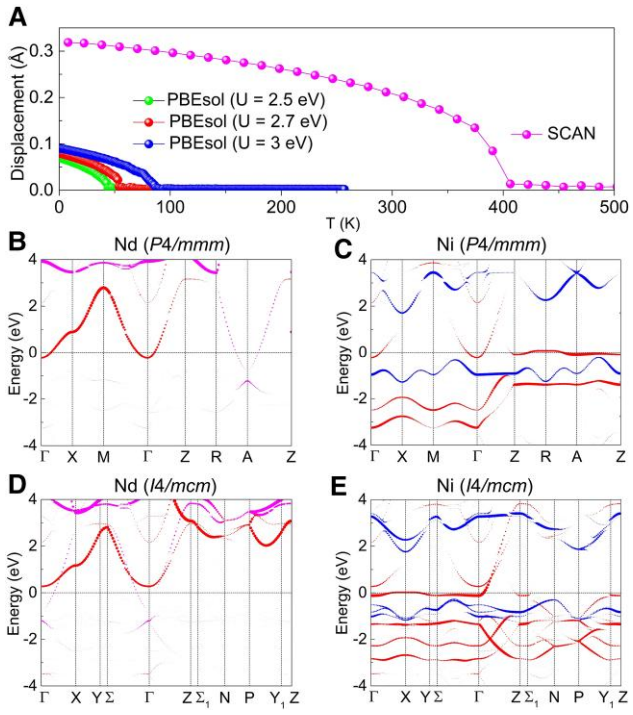

Fig. 3. Finite-temperature properties of $NdNiO_2$. A) Rotation motion induced displacement of oxygen atoms relative to the *P4/mmm* phase as a function of temperature obtained from PBEsol + U and SCAN methods. The orbital-projected band structure with orbital character of B) Nd d_{xy} (magenta) and $d_{3z^2-r^2}$ (red) states and C) Ni $d_{3z^2-r^2}$ (red) and $d_{x^2-y^2}$ (blue) states in the C-AFM *P4/mmm* phase calculated by PBEsol + U (U = 2.7 eV). The corresponding orbital-projected band structure of Nd and Ni atoms in the *I4/mcm* phase are shown in D) and E), respectively. The Fermi level denoted by the dash line is set to zero energy.

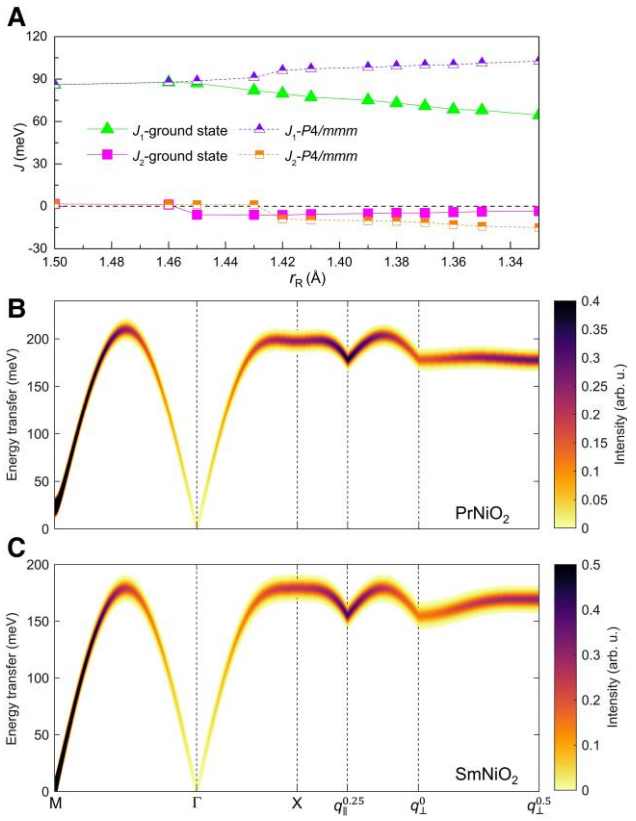

Fig. 4. *R*-site cation determined magnetic properties of $RNiO_2$. A) First-neighbor in-plane (J_1) and out-of-plane (J_2) exchange constants for different $RNiO_2$ compounds in the *P4/mmm* and *I4/mcm* phases. The simulated adiabatic spin-wave dispersions of B) $PrNiO_2$ and C) $SmNiO_2$. Here, M = (0.5, 0.5, 0), Γ = (0, 0, 0), X = (0.5, 0, 0), $q_{\parallel}^{0.25}$ = (0.5, 0.25, 0), $q_{\perp}^{0}$ = (0.25, 0, 0), and $q_{\perp}^{0.5}$ = (0.25, 0, 0.5).

line with superconducting LaOFeAs (47) and $Sr_3Rh_4Sn_{13}$ (48), the resistivity anomaly observed at low temperature in $NdNiO_2$ (1) and absent in $LaNiO_2$ (dynamical stable in the magnetic *P4/mmm* phase) might be attributed to the structural phase transition. The results in Fig. 3A indicate that T_R gradually increases as U increases. As larger U values (4–5 eV) and the SCAN functional largely overestimate the transition temperature, a relatively small U of 2.7 eV is employed in our work.

Rare-earth control of magnetic transition

Figure 4A shows the variation of first-neighbor exchange constants across the $RNiO_2$ series in the ground state phases and high-symmetry *P4/mmm* phase. In terms of first-neighbor out-of-plane exchange constant, we see an abrupt change around the phase boundary in the ground state phases, $LaNiO_2$ and $PrNiO_2$ exhibit negligible out-of-plane magnetic coupling, similar with cuprate superconductors (65). In contrast, $RNiO_2$ with R = Nd–Lu possess the 3D magnetic interactions with nonnegligible out-of-plane FM magnetic coupling, similar with iron superconductors (66–68). In order to confirm how the rare-earth ion controls the magnetic dimensionality, the magnetic excitation dispersion of $PrNiO_2$ and $SmNiO_2$ are compared in Fig. 4B and C, respectively. The spectra of $PrNiO_2$ exhibits similar characters as the recent resonant inelastic X-ray scattering (RIXS) experiment (40), indicating that the employed long-range magnetic order is a good approximation of the experimental results. The negligible and nonnegligible dispersion along the out-of-plane (0.25, 0, 0)–(0.25, 0, 0.5) path (measured in the RIXS experiment of $NdNiO_2$ (4)) in $PrNiO_2$ and $SmNiO_2$ imply their quasi-2D AFM and 3D-AFM nature. Consequently, rare-earth ion not only controls the magnetic order, but also the magnetic dimensionality of $RNiO_2$.

Spin-rotation coupling determined in-plane exchange constants

It is generally believed that superconductivity in iron and cuprate superconductors is related to the in-plane AFM coupling. Moreover, the rare-earth element is a key factor affecting the superconducting temperature (69, 70). It is thus important to evaluate the variation of dominant exchange constants across the $RNiO_2$ series.

Typically, the magnetic coupling in ABX_3 perovskites strongly depends on the variation of lattice constant and rotation angle (71): when the radius of A-site cation decreases, the lattice constants decrease while the rotation angle gradually increases. The reduction of the lattice constants typically enhances the magnetic coupling, while the increase in rotation weakens the magnetic interaction (71), thus, the actual influence of A-site cation on the exchange constants is determined by the competing effects of lattice constants and rotation. In $RNiO_2$, the decrease in the *R*-site cation radius also gives rise to a decrease in the lattice constants and an increase in rotation in a similar way as ABX_3 perovskites (71). It can thus be expected that taking only into account the influence of lattice constant evolution on the exchange

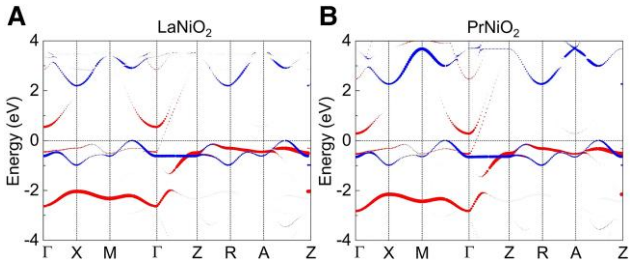

Fig. 5. Electronic structure in quasi-2D AFM $RNiO_2$. The orbital-projected band structure with orbital character of Ni $d_{3z^2-r^2}$ (red) and $d_{x^2-y^2}$ (blue) states for A) $LaNiO_2$ and B) $PrNiO_2$.

coupling, as considered in previous works (19, 23), is not enough to describe the global effect of *R*-site cation substitution: the additional effect of oxygen rotation amplitudes must be taken into account.

Figure 4A also displays the exchange constants in the high-symmetry *P*4/*mmm* phases without rotation, we found that the in-plane first-neighbor magnetic coupling is progressively increased when decreasing r_R, similar to recent work (23). In contrast, we obtain an almost opposite trend for the in-plane AFM coupling in the ground state *I*4/*mcm* phase compared with (23) as it gradually decreases as r_R decreases when R = Nd–Lu as shown in Fig. 4A. Therefore, the decreased in-plane AFM coupling for smaller r_R in the ground state *I*4/*mcm* phase should be attributed to the increase in rotation, whose effect is partly compensated by the lattice constants effect. The r_R dependent AFM coupling is completely in line with rare-earth perovskites like $RCrO_3$ (72), $RFeO_3$ (73), and $RNiO_3$ (74), indicating that rare-earth ions in infinite-layer nickelates affect the magnetic interactions through spin-rotation coupling.

Rare-earth control of electronic transition

To account for the electronic origin of magnetic transition in $RNiO_2$, we then compare the orbital-projected band structure of $LaNiO_2$ and $PrNiO_2$ in Fig. 5 with that of $NdNiO_2$ in Fig. 3E. Strikingly, there is a sudden reconstruction of the Fermi surface coinciding with the magnetic transition. The decrease in r_R from La(Pr)NiO_2 to $NdNiO_2$ shifts the band edge of $d_{3z^2-r^2}$ orbital to a higher energy than the Fermi level. The dominated states at the Fermi level have changed from $d_{x^2-y^2}$ bands to $d_{3z^2-r^2}$ bands, which is characteristic of an electronic transition. The electronic structure of $NdNiO_2$ is in line with previous works (19, 20, 21, 22, 75) and reminiscent of the orbital-selective localization as found in alkaline iron selenides (76, 77) and $(Ca,Sr)_2RuO_4$ (78, 79), which is also suggested in previous works (9–12, 80).

Table 1 compares the orbital contributed first-neighbor exchange constants among $LaNiO_2$, $PrNiO_2$, $NdNiO_2$, and $SmNiO_2$. The predicted exchange constants for $PrNiO_2$ and $NdNiO_2$ are very close to the experimental results (4, 40). Moreover, the first-neighbor in-plane exchange constants in different compounds are all mainly contributed by the interactions between nearest-neighbor Ni $d_{x^2-y^2}$ orbitals, whereas the Ni $d_{3z^2-r^2}$ orbital is responsible for the out-of-plane FM coupling in $NdNiO_2$ and $SmNiO_2$. Consequently, the quasi-2D and 3D magnetic dimensionality in La(Pr)NiO_2 and Nd(Sm)NiO_2 lies in the absence and presence of spin-polarized $d_{3z^2-r^2}$ electrons at the Fermi level.

Rare-earth control of upper critical magnetic

The unexpected isotropy of the upper critical magnetic field H_{c2} is recently revealed in experiments (5, 6, 39). Ferropnictides are multiband superconductors with both Mott-localized and itinerant electrons (66–68, 81, 82), similar with 3D C-AFM $NdNiO_2$. It has been revealed that k_z dispersion naturally facilitates the circulating currents at all field orientations and results in the isotropic H_{c2} as found in ferropnictides (46). Interestingly, the band structure of $NdNiO_2$ shown in Fig. 3E shows a strong k_z dispersion denoted by the large weight of the Ni $d_{3z^2-r^2}$ band at the Fermi level. In contrast, there is rather weak k_z dispersion at the Fermi level for $LaNiO_2$ (Fig. 5A) and $PrNiO_2$ (Fig. 5B) as reflected by the small weight of the Ni $d_{3z^2-r^2}$ band. Therefore, our results support the fact that the strength of k_z dispersion in $NdNiO_2$ and La(Pr)NiO_2 are likely responsible for their isotropic and anisotropic H_{c2} observed in experiments.

Structural origin of magnetic and electronic transitions

In order to disentangle the microscopic mechanism behind the *R*-site cation controlled electronic and magnetic transitions, we focus on the structural effect induced by rare-earth ion. The variation of in-plane and out-of-plane lattice constants are compared in Fig. 6A. As r_R decreases, despite the in-plane and out-of-plane lattice constants both progressively decrease, the reduction of out-of-plane lattice constant is much faster than that of in-plane lattice constants consistent with previous work (23). Thus, the decrease in rare-earth ionic radius reduces the *c*/*a* ratio analogous to that of epitaxial biaxial tensile strain.

From the above analysis, we notice that the main difference between 2D-AFM La(Pr)NiO_2 and 3D C-AFM Nd(Sm)NiO_2 arises from the itinerant $d_{3z^2-r^2}$ bands, which is spin-polarized and has a higher energy level than the $d_{x^2-y^2}$ bands in the 3D C-AFM state. In ABX_3 perovskites, epitaxial biaxial tensile strain directly yields the elongation and contraction of the in-plane and out-of-plane lattice constant, respectively. Such effect typically weakens and strengthens the hybridization of $d_{x^2-y^2}$ and $d_{3z^2-r^2}$ bands with the surrounding O *p* orbitals. As a result, the on-site energy of $d_{x^2-y^2}$ and $d_{3z^2-r^2}$ orbitals will shift to a lower and higher energy level, respectively (83).

The strain-orbital relationship in perovskites could be naturally extended to infinite-layer nickelates and is indispensable to rationalize the *R*-site cation-tuned electronic and magnetic transitions. The evolution of electronic structure and direct

Table 1. First-neighbor exchange constants and their orbital contributions for $LaNiO_2$, $PrNiO_2$, $NdNiO_2$, and $SmNiO_2$ in the unit of meV. The dominant contributions to the first-neighbor in-plane magnetic interactions are labeled in bold.

	Total	$d_{x^2-y^2}-d_{x^2-y^2}$	$d_{x^2-y^2}-d_{xy}$	$d_{3z^2-r^2}-d_{3z^2-r^2}$	$d_{x^2-y^2}-d_{3z^2-r^2}$	$d_{xy}-d_{xy}$	$d_{xz}-d_{xz}$	$d_{yz}-d_{yz}$
J_1 ($LaNiO_2$)	85.98	**85.80**	0.00	0.10	0.16	0.00	0.06	−0.14
J_1 ($PrNiO_2$)	87.24	**87.05**	0.00	0.20	0.11	0.00	0.08	−0.20
J_1 ($NdNiO_2$)	87.07	**82.93**	2.98	0.29	0.74	0.10	0.06	−0.03
J_2 (($NdNiO_2$)	−5.98	−0.26	−0.02	−6.10	0.00	0.04	0.18	0.18
J_1 ($SmNiO_2$)	82.03	**74.11**	6.67	0.34	0.59	0.29	0.05	−0.02
J_2 (($SmNiO_2$)	−6.01	−0.17	−0.04	−6.16	0.00	0.04	0.16	0.16

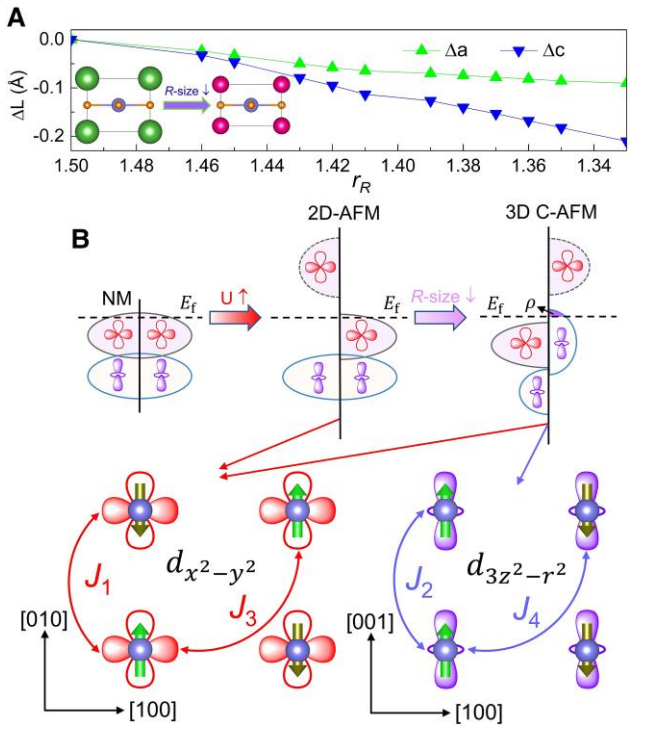

Fig. 6. Structural origin of magnetic and electronic transitions. A) Evolution of in-plane and out-of-plane lattice constants of $RNiO_2$ relative to $LaNiO_2$. The inset atomic structures denote that the reduction of rare-earth size decreases the c/a ratio, which is analogous to the effect of epitaxial biaxial tensile strain. B) Schematic of the interplay among lattice, electron, and spin degrees of freedom. E_f, Fermi level; U, Hubbard U value of *d* electron; ρ, the unoccupied $d_{3z^2-r^2}$ state; ↑ and ↓ denote increase and decrease, respectively.

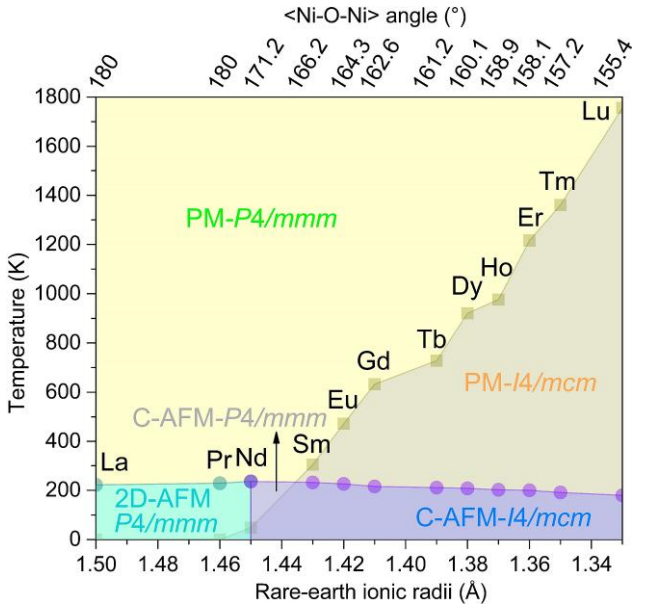

Fig. 7. Phase diagram of infinite-layer nickelates in terms of rare-earth ionic radii and the temperature with PBEsol + *U* (*U* = 2.7 eV). The circles refer to the AFM–PM transition temperature and the squares represent the transition temperature from the *I*4/*mcm* phase to the *P*4/*mmm* phase.

structure–electron–magnetism relationship are schematically shown in Figs. 6B and S5.

In the nonmagnetic state, the out-of-plane $d_{3z^2-r^2}$ state is lower than the in-plane $d_{x^2-y^2}$ state due to the crystal field, and is almost fully occupied by a pair of electrons (also see Fig. S5A). The reduction of the bandwidth of partly occupied $d_{x^2-y^2}$ bands by the electron–electron interaction *U* gives rise to a spin Mott splitting, which shifts the majority and minority spin channel below and above the Fermi energy for *R* = La–Pr (also see Fig. S5B). The spin splitting of $d_{x^2-y^2}$ bands at the Fermi surface results in the 2D-AFM state with mainly in-plane magnetic interactions. As the reduction of the rare-earth size gradually decreases the *c*/*a* ratio, the hybridization between the interlayer Ni $d_{3z^2-r^2}$ orbital and their on-site energy is increased. Consequently, the Ni $d_{3z^2-r^2}$ bands become spin polarized and occupy the Fermi level for *R* = Nd–Lu. (also see Fig. S5C) Since the spin-polarized $d_{3z^2-r^2}$ electrons are decisive for the out-of-plane FM magnetic coupling (also see Table 1), the geometrical effect controlled electronic transition is correspondingly accompanied by the change in magnetic dimensionality. The results are based on the density functional theory (DFT) + *U* ground state calculations, to further investigate the electronic structure in high-temperature PM phase and quantum many-body effects, dynamical mean field theory (DMFT) (14–17, 13, 18) method should be employed.

Phase diagram of $RNiO_2$ compounds

Combining the Néel temperature obtained from the Monte Carlo simulations of the Heisenberg spin Hamiltonian and structural transition temperature determined by the second-principles model, the temperature-dependent structural and magnetic transitions of the whole family of $RNiO_2$ compounds are summarized in the global phase diagram reported in Fig. 7. Except for high-symmetry $LaNiO_2$ and $PrNiO_2$, we see that all the other infinite-layer nickelate compounds undergo a structural phase transition from the low-symmetry *I*4/*mcm* phase to the high-symmetry *P*4/*mmm* phase. Moreover, as rare-earth ionic radii r_R decreases, the transition temperature T_R continuously increases from $NdNiO_2$ to $LuNiO_2$ due to the more distorted structure, as similarly observed in $RNiO_3$ perovskites (50).

Owning to the decreased in-plane first-neighbor exchange constant from $NdNiO_2$ to $LuNiO_2$, it is found that the AFM–PM transition temperature T_N decreases steadily as r_R decreases (except the high-symmetry $LaNiO_2$ and $PrNiO_2$) which is also strongly analogous to the behavior observed in $RNiO_3$ (*R* = Sm–Lu) perovskites (84). Consequently, the presence of rotation motion not only affects the electronic property and the overall magnitude of the magnetic transition temperature, but gives rise to a much more complex phase diagram with five distinct phases: (i) the 2D-AFM high-symmetry *P*4/*mmm* phase, (ii) the C-AFM low-symmetry *I*4/*mcm* phase, (iii) the C-AFM high-symmetry *P*4/*mmm* phase, (iv) the PM low-symmetry *I*4/*mcm* phase, and (v) the PM high-symmetry *P*4/*mmm* phase. The complex phase diagram of infinite-layer nickelates shows strong similarities with the phase diagram of perovskite nickelates and the dedicated interplay among the spin, electron, rotation, and temperature opens new perspectives for the control of magnetic and superconducting properties by exploiting the different strategies previously used in perovskite nickelates.

Conclusion and outlook

In summary, we present a systematic theoretical investigation of the effect of rare-earth ions by explicitly exploring the interplay among the structural, electronic, and magnetic degrees of

freedom in infinite-layer nickelates. Structurally, we reveal that oxygen rotation distortion is destabilized with reducing rare-earth size and strengthened by magnetism, which triggers a phase transition from $P4/mmm$ to $I4/mcm$ at low temperature for $RNiO_2$ (R = Nd–Lu). The rotation motion appears to be the key to provide a consistent description of the structural, electronic, and magnetic properties of infinite layers. First, it strongly suppresses the self-doping effect, which can explain the unusual upturn of resistivity in $NdNiO_2$ observed at low temperature (1). Second, the rotation has to be included to provide a proper description of the evolution of the magnetic coupling strength in $RNiO_2$.

From electronic and magnetic viewpoints, reducing the rare-earth size plays a similar role as epitaxial tensile strain, which strongly affects the competition between localized Ni $d_{x^2-y^2}$ electrons and itinerant Ni $d_{3z^2-r^2}$ electrons, magnetic coupling strength, and magnetic dimensionality, resulting in two possible ground states. Compounds with larger c/a ratio such as $LaNiO_2$ and $PrNiO_2$ resemble the key electronic and magnetic properties of $CaCuO_2$. However, compounds with smaller c/a ratio (R = Nd–Lu) show marked electronic and magnetic resemblance to ferropnictides with notable interlayer FM coupling and strong k_z dispersion, which may help elucidate the small anisotropy of the upper critical field of $NdNiO_2$ observed experimentally.

Based on the actual interplay among different factors, we eventually build a global and clear theoretical description of the lattice–electron–spin relationship. Accordingly, a complete phase diagram summarizing the temperature evolution of structural and magnetic phases in the whole family of $RNiO_2$ compounds is established. Our work not only provides a deeper fundamental understanding of $RNiO_2$ compounds that explicitly combines the interplay among different degrees of freedom, but also exploits this knowledge to explain the rare-earth control of resistivity and upper critical magnetic field observed in experiments. As such, we hope that our work could motivate experimentalists to further exploit the coupling among rotation, charge, orbital, spin, and strain degrees of freedom in infinite layer $RNiO_2$ to realize the optimization of the applications as superconductors.

Methods

First-principles calculations

Our DFT plus U ($U = 2.7$ eV) calculations (63) were carried out using the projector augmented wave (PAW) method implemented in Vienna ab initio simulation package (VASP) (85, 86). The revised Perdew–Becke–Erzenhof functional for solids (PBEsol) (62) was employed. For the structural relaxation, the energy and Hellmann–Feynman forces tolerance were set to be 10^{-7} eV and 10^{-3} eV/Å, respectively. The kinetic energy cutoff of the plane-wave basis was 700 eV and the Brillouin-zone integrations were sampled by $9 \times 9 \times 7$ Γ-centered k-point mesh (87). The phonon dispersion calculations were performed using the finite displacement method as implemented in the PHONOPY code (88).

Second-principles calculation

First-principles based second-principles method is applied to investigate the evolution of rotation motion at different temperatures. We build a second-principles model with displacements of oxygen atom μ as the degree of freedom. The total energy can be expressed as

$$E_{total} = E_{self} + E_{short} \quad (1)$$

Where $E(\mu_i)$ in the first term $E_{self} = \sum_i E(\mu_i)$ represents the energy of an isolated oxygen atom at ith location with amplitude μ_i. It is truncated at fourth order, and the maximum energy difference between our model and DFT is smaller than 1 meV per unit cell, which indicates this model is good enough to describe the PESs. Due to the symmetry consideration, $E(\mu_i)$ can be written as

$$E(\mu_i) = k_1\mu_i^2 + k_2\mu_i^4 \quad (2)$$

Where k_1 and k_2 refer to the parameters to be determined from first-principles calculations by fitting the total energy of structures with eight different modes shown in Fig. S6A to P. In the second term $E_{short} = \sum_{i,j} g_{ij}\mu_i\mu_j$, μ_i and μ_j are the amplitude of oxygen atom displacements at ith and jth location and g_{ij} is the coupling parameter between them. This term is the energy contribution from the short-range interactions between neighboring oxygen atoms. The length of short-range interactions is truncated at one unit cell. Due to the symmetry consideration, there are only four independent interaction parameters (g_1, g_2, g_3, and g_4) for the short-range interactions as sketched in Fig. S6Q and R. All these parameters are obtained from first-principles calculations. Based on the second-principles model, the Monte Carlo simulations are carried out to investigate the rotation motion with a heating run from 0 to 2000 K in steps of 1 K. For each temperature steps, 100,000 Monte Carlo steps are performed. The calculations were performed on a $12 \times 12 \times 12$ supercell. To guarantee an acceptance ratio of 0.2, the step sizes are adjusted accordingly. The total energies obtained from first-principles calculations and second-principles model are compared in Fig. S6S. The close match of the energies guarantees the accuracy and validity of our model.

Exchange constant and magnetic excitations calculations

The exchange constants and the orbital contributions were calculated by using the TB2J code (89). In this approach, magnetic force theorem (90) is implemented based on the maximally localized Wannier functions (91, 92), which were built from the DFT band structure. The Nd d_{xy} and $d_{3z^2-r^2}$ orbitals, Ni d_{xy}, d_{yz}, d_{zx}, $d_{x^2-y^2}$, and $d_{3z^2-r^2}$ orbitals and O p_x, p_y, and p_z orbitals are used for constructing the Wannier functions. The Heisenberg Hamiltonian in the TB2J code is

$$H = \sum_{\langle i,j \rangle} J_{ij} S_i S_j \quad (3)$$

where J_{ij} denotes the exchange constant at any order and $S = 1/2$ spin. The spin-wave spectra is calculated by the SpinW program (93) based on the obtained exchange constants.

Supplementary Material

Supplementary material is available at *PNAS Nexus* online.

Funding

The work is supported by the Initial Scientific Research Fund of Lanzhou University for Young Researcher Fellow (Grant No. 561120206) and the National Natural Science Foundation of China (Grant No. 12102157). Y.Z. acknowledge the Computational support by the Center for Computational Science and Engineering of Lanzhou University and Southern University of Science and Technology. Ph.G. and X.H. acknowledge financial support from F.R.S.-FNRS Belgium through the PDR project PROMOSPAN (grant T.0107.20).

Author contributions

Y.Z. and P.G. designed research; Y.Z. and J.Z. did the simulations; and Y.Z wrote the paper; X.H. and J.W. participated in designing the project and simulations.

Data availability

All data are contained within the manuscript.

References

1 Li D, *et al.* 2019. Superconductivity in an infinite-layer nickelate. *Nature*. 572(7771):624–627.
2 Osada M, *et al.* 2020. A superconducting praseodymium nickelate with infinite layer structure. *Nano Lett*. 20(8):5735–5740.
3 Hepting M, *et al.* 2020. Electronic structure of the parent compound of superconducting infinite-layer nickelates. *Nat Mater*. 19(4):381–385.
4 Lu H, *et al.* 2021. Magnetic excitations in infinite-layer nickelates. *Science*. 373(6551):213–216.
5 Wang BY, *et al.* 2021. Isotropic pauli-limited superconductivity in the infinite-layer nickelate $Nd_{0.775}Sr_{0.225}NiO_2$. *Nat Phys*. 17(4): 473–477.
6 Xiang Y, *et al.* 2021. Physical properties revealed by transport measurements for superconducting $Nd_{0.8}Sr_{0.2}NiO_2$ thin films. *Chin Phys Lett*. 38(4):047401.
7 Li D, *et al.* 2020. Superconducting dome in $Nd_{1-x}Sr_xNiO_2$ infinite layer films. *Phys Rev Lett*. 125(2):027001.
8 Zeng S, *et al.* 2020. Phase diagram and superconducting dome of infinite-layer $Nd_{1-x}Sr_xNiO_2$ thin films. *Phys Rev Lett*. 125(14): 147003.
9 Lechermann F. 2020. Multiorbital processes rule the $Nd_{1-x}Sr_xNiO_2$ normal state. *Phys Rev X*. 10(4):041002.
10 Lechermann F. 2020. Late transition metal oxides with infinite-layer structure: nickelates versus cuprates. *Phys Rev B*. 101(8): 081110.
11 Botana AS, Norman MR. 2020. Similarities and differences between $LaNiO_2$ and $CaCuO_2$ and implications for superconductivity. *Phys Rev X*. 10(1):011024.
12 Adhikary P, Bandyopadhyay S, Das T, Dasgupta I, Saha-Dasgupta T. 2020. Orbital-selective superconductivity in a two-band model of infinite-layer nickelates. *Phys Rev B*. 102(10):100501.
13 Werner P, Hoshino S. 2020. Nickelate superconductors: multiorbital nature and spin freezing. *Phys Rev B*. 101(4):041104.
14 Leonov I, Skornyakov SL, Savrasov SY. 2020. Lifshitz transition and frustration of magnetic moments in infinite-layer $NdNiO_2$ upon hole doping. *Phys Rev B*. 101(24):241108.
15 Karp J, *et al.* 2020. Many-body electronic structure of $NdNiO_2$ and $CaCuO_2$. *Phys Rev X*. 10(2):021061.
16 Chen D, Jiang P, Si L, Lu Y, Zhong Z. 2022. Magnetism in doped infinite-layer $NdNiO_2$ studied by combined density functional theory and dynamical mean-field theory. *Phys Rev B*. 106(4): 045105.
17 Ryee S, Yoon H, Kim TJ, Jeong MY, Han MJ. 2020. Induced magnetic two-dimensionality by hole doping in the superconducting infinite-layer nickelate $Nd_{1-x}Sr_xNiO_2$. *Phys Rev B*. 101(6):064513.
18 Petocchi F, Christiansson V, Nilsson F, Aryasetiawan F, Werner P. 2020. Normal state of $Nd_{1-x}Sr_xNiO_2$ from self-consistent GW+ EDMFT. *Phys Rev X*. 10(4):041047.
19 Kapeghian J, Botana AS. 2020. Electronic structure and magnetism in infinite-layer nickelates $RNiO_2$ (R = La–Lu). *Phys Rev B*. 102-(20):205130.
20 Choi M-Y, Pickett WE, Lee K-W. 2020. Fluctuation-frustrated flat band instabilities in $NdNiO_2$. *Phys Rev Res*. 2(3):033445.
21 Zhang R, *et al.* 2021. Magnetic and f-electron effects in $LaNiO_2$ and $NdNiO_2$ nickelates with cuprate-like band. *Commun Phys*. 4(1):1–12.
22 Lechermann F. 2021. Doping-dependent character and possible magnetic ordering of $NdNiO_2$. *Phys Rev Mater*. 5(4):044803.
23 Been E, *et al.* 2021. Electronic structure trends across the rare-earth series in superconducting infinite-layer nickelates. *Phys Rev X*. 11(1):011050.
24 Choi M-Y, Lee K-W, Pickett WE. 2020. Role of 4f states in infinite-layer $NdNiO_2$. *Phys Rev B*. 101(2):020503.
25 Wan X, Ivanov V, Resta G, Leonov I, Savrasov SY. 2021. Exchange interactions and sensitivity of the Ni two-hole spin state to Hund's coupling in doped $NdNiO_2$. *Phys Rev B*. 103(7):075123.
26 Liu Z, Ren Z, Zhu W, Wang Z, Yang J. 2020. Electronic and magnetic structure of infinite-layer $NdNiO_2$ trace of antiferromagnetic metal. *npj Quantum Mater*. 5(1):1–8.
27 Nomura Y, *et al.* 2019. Formation of a two-dimensional single-component correlated electron system and band engineering in the nickelate superconductor $NdNiO_2$. *Phys Rev B*. 100(20): 205138.
28 Xia C, Wu J, Chen Y, Chen H. 2022. Dynamical structural instability and its implications for the physical properties of infinite-layer nickelates. *Phys Rev B*. 105(11):115134.
29 Bernardini 3, Bosin A, Cano A. 2022. Geometric effects in the infinite-layer nickelates. *Phys Rev Mater*. 6(4):044807.
30 2022. Structural instabilities of infinite-layer nickelates from first-principles simulations. *Phys Rev Res*. 4(2):023064.
31 Jiang Mi, Berciu M, Sawatzky GA. 2020. Critical nature of the Ni spin state in doped $NdNiO_2$. *Phys Rev Lett*. 124(20):207004.
32 Wu X, *et al.* 2020. Robust $d_{x^2-y^2}$-wave superconductivity of infinite-layer nickelates. *Phys Rev B*. 101(6):060504.
33 Klett M, Hansmann P, Schäfer T. 2022. Magnetic properties and pseudogap formation in infinite-layer nickelates: insights from the single-band hubbard model. *Front Phys*. 10:45.
34 Wang Z, Zhang G-M, Yang Y-F, Zhang F-C. 2020. Distinct pairing symmetries of superconductivity in infinite-layer nickelates. *Phys Rev B*. 102(22):220501.
35 Goodge BH, *et al.* 2021. Doping evolution of the Mott–Hubbard landscape in infinite-layer nickelates. *Proc Natl Acad Sci USA*. 118(2):e2007683118.
36 Tam CC, *et al.* 2022. Charge density waves in infinite-layer $NdNiO_2$ nickelates. *Nat Mater*. 21:1116–1120.
37 Malyi OI, Varignon J, Zunger A. 2022. Bulk $NdNiO_2$ is thermodynamically unstable with respect to decomposition while hydrogenation reduces the instability and transforms it from metal to insulator. *Phys Rev B*. 105(1):014106.
38 Fowlie J, *et al.* 2022. Intrinsic magnetism in superconducting infinite-layer nickelates. *Nat Phys*. 18(4):1043–1047.
39 Wang BY, *et al.* 2022. Rare-earth control of the superconducting upper critical field in infinite-layer nickelates. arXiv, arXiv:2205.15355, preprint: not peer reviewed.
40 Gao Q, *et al.* 2022. Magnetic excitations in strained infinite-layer nickelate $PrNiO_2$. arXiv, arXiv:2208.05614, preprint: not peer reviewed.
41 Been EM, *et al.* 2022. On the nature of valence charge and spin excitations via multi-orbital Hubbard models for infinite-layer nickelates. *Front Phys*. 10:836959.
42 Xie TY, *et al.* 2022. Microscopic theory of superconducting phase diagram in infinite-layer nickelates. *Phys Rev B*. 106(3):035111.

43 Kreisel A, Andersen B M, Rømer A T, Eremin IM, Lechermann F. 2022. Superconducting instabilities in strongly correlated infinite-layer nickelates. *Phys Rev Lett*. 129(7):077002.
44 Catalano S, *et al.* 2018. Rare-earth nickelates $RNiO_3$: thin films and heterostructures. *Rep Prog Phys*. 81(4):046501.
45 Middey S, *et al.* 2016. Physics of ultrathin films and heterostructures of rare-earth nickelates. *Annu Rev Mater Res*. 46:305–334.
46 Yuan HQ, *et al.* 2009. Nearly isotropic superconductivity in (Ba, K) Fe_2As_2. *Nature*. 457(7229):565–568.
47 de La Cruz C, *et al.* 2008. Magnetic order close to superconductivity in the iron-based layered $LaO_{1-x}F_xFeAs$ systems. *Nature*. 453-(7197):899–902.
48 Goh SK, *et al.* 2015. Ambient pressure structural quantum critical point in the phase diagram of $(Ca_xSr_{1-x})_3Rh_4Sn_{13}$. *Phys Rev Lett*. 114(9):097002.
49 Zhou JS, Goodenough JB. 2004. Chemical bonding and electronic structure of $RNiO_3$ R = rare earth). *Phys Rev B*. 69(15):153105.
50 Mercy A, Bieder J, Íñiguez J, Ghosez P. 2017. Structurally triggered metal-insulator transition in rare-earth nickelates. *Nat Commun*. 8(1):1–6.
51 Peil OE, Hampel A, Ederer C, Georges A. 2019. Mechanism and control parameters of the coupled structural and metal-insulator transition in nickelates. *Phys Rev B*. 99(24): 245127.
52 Hampel A, Liu P, Franchini C, Ederer C. 2019. Energetics of the coupled electronic-structural transition in the rare-earth nickelates. *npj Quantum Mater*. 4(1):1–7.
53 Georgescu AB, Peil OE, Disa AS, Georges A, Millis AJ. 2019. Disentangling lattice and electronic contributions to the metal-insulator transition from bulk vs. layer confined $RNiO_3$. *Proc Natl Acad Sci USA*. 116(29):14434–14439.
54 Liao Z, *et al.* 2018. Metal-insulator-transition engineering by modulation tilt-control in perovskite nickelates for room temperature optical switching. *Proc Natl Acad Sci USA*. 115(38): 9515–9520.
55 Varignon, Grisolia MN, Íñiguez J, Barthélémy A, Bibes M. 2017. Complete phase diagram of rare-earth nickelates from first-principles. *npj Quantum Mater*. 2(1):1–9.
56 Wojdeł JC, Hermet P, Ljungberg MP, Ghosez P, Iniguez J67. 2013. First-principles model potentials for lattice-dynamical studies: general methodology and example of application to ferroic perovskite oxides. *J Phys: Condens Matter*. 25(30):305401.
57 Zhong W, Vanderbilt D, Rabe KM. 1994. Phase transitions in $BaTiO_3$ from first principles. *Phys Rev Lett*. 73(13):1861.
58 Hui Q, Tucker MG, Dove MT, Wells SA, Keen DA. 2005. Total scattering and reverse monte carlo study of the 105 K displacive phase transition in strontium titanate. *J Phys: Condens Matter*. 17(5):S111.
59 Klarbring J, Simak SI. 2018. Nature of the octahedral tilting phase transitions in perovskites: a case study of $CaMnO_3$. *Phys Rev B*. 97(2):024108.
60 Radin MD, Thomas JC, Van der Ven A. 2020. Order-disorder versus displacive transitions in Jahn-Teller active layered materials. *Phys Rev Mater*. 4(4):043601.
61 Zhong W, Vanderbilt D, Rabe KM. 1995. First-principles theory of ferroelectric phase transitions for perovskites: the case of $BaTiO_3$. *Phys Rev B*. 52(9):6301.
62 Perdew JP, *et al.* 2008. Restoring the density-gradient expansion for exchange in solids and surfaces. *Phys Rev Lett*. 100(13):136406.
63 Dudarev SL, Botton GA, Savrasov SY, Humphreys CJ, Sutton AP. 1998. Electron-energy-loss spectra and the structural stability of nickel oxide: an LSDA + U study. *Phys Rev B*. 57(3):1505.
64 Pizzi G, Volja D, Kozinsky B, Fornari M, Marzari N. 2014. Boltzwann: a code for the evaluation of thermoelectric and electronic transport properties with a maximally-localized Wannier functions basis. *Comput Phys Commun*. 185(1):422–429.
65 Endoh Y, *et al.* 1988. Static and dynamic spin correlations in pure and doped La_2CuO_4. *Phys Rev B*. 37(13):7443.
66 Zhao J, *et al.* 2009. Spin waves and magnetic exchange interactions in $CaFe_2As_2$. *Nat Phys*. 5(8):555–560.
67 Dai P, Hu J, Dagotto E. 2012. Magnetism and its microscopic origin in iron-based high-temperature superconductors. *Nat Phys*. 8(10): 709–718.
68 McQueeney RJ, *et al.* 2008. Anisotropic three-dimensional magnetism in $CaFe_2As_2$. *Phys Rev Lett*. 101(22):227205.
69 Fisk Z, Thompson JD, Zirngiebl E, Smith JL, Cheong S-W. 1987. Superconductivity of rare earth-barium-copper oxides. *Solid State Commun*. 62(11):743–744.
70 Ren Z-A, *et al.* 2008. Superconductivity and phase diagram in iron-based arsenic-oxides $ReFeAsO_{1-\delta}$ (Re = rare-earth metal) without fluorine doping. *Europhys Lett*. 83(1):17002.
71 Fedorova NS, *et al.* 2018. Relationship between crystal structure and multiferroic orders in orthorhombic perovskite manganites. *Phys Rev Mater*. 2(10):104414.
72 Hornreich RM. 1978. Magnetic interactions and weak ferromagnetism in the rare-earth orthochromites. *J Magn Magn Mater*. 7(1–4):280–285.
73 Treves D, Eibschutz M, Coppens P. 1965. Dependence of superexchange interaction on Fe^{3+}-O^{2-}-FE^{3+} linkage angle. *Phys Lett*. 18: 216.
74 Medarde ML. 1997. Structural, magnetic and electronic properties of perovskites (R = rare earth). *J Phys: Condens Matter*. 9(8):1679.
75 Lang Z-J, Jiang R, Ku W. 2021. Strongly correlated doped hole carriers in the superconducting nickelates: their location, local many-body state, and low-energy effective Hamiltonian. *Phys Rev B*. 103(18):L180502.
76 Yu R, Si Q. 2013. Orbital-selective Mott phase in multiorbital models for alkaline iron selenides $K_{1-x}Fe_{2-y}Se_2$. *Phys Rev Lett*. 110-(14):146402.
77 Yi M, *et al.* 2013. Observation of temperature-induced crossover to an orbital-selective Mott phase in $A_xFe_{2-y}Se_2$ (A = K, Rb) superconductors. *Phys Rev Lett*. 110(6):067003.
78 Anisimov VI, Nekrasov IA, Kondakov DE, Rice TM, Sigrist M. 2002. Orbital-selective Mott-insulator transition in $Ca_{2-x}Sr_xRuO_4$. *Eur Phys J B*. 25(2):191–201.
79 de'Medici L, Hassan SR, Capone M, Dai X. 2009. Orbital-selective Mott transition out of band degeneracy lifting. *Phys Rev Lett*. 102-(12):126401.
80 Lee K-W, Pickett WE. 2004. Infinite-layer $LaNiO_2$: Ni^{1+} is not Cu^{2+}. *Phys Rev B*. 70(16):165109.
81 Misawa T, Nakamura K, Imada M. 2012. Ab initio evidence for strong correlation associated with Mott proximity in iron-based superconductors. *Phys Rev Lett*. 108(17):177007.
82 Kou S-P, Li T, Weng ZY. 2009. Coexistence of itinerant electrons and local moments in iron-based superconductors. *Europhys Lett*. 88(1):17010.
83 Nanda BRK, Satpathy S. 2008. Effects of strain on orbital ordering and magnetism at perovskite oxide interfaces: $LaMnO_3/SrMnO_3$. *Phys Rev B*. 78(5):054427.
84 Zhou J-S, Goodenough JB, Dabrowski B. 2005. Exchange interaction in the insulating phase of $RNiO_3$. *Phys Rev Lett*. 95(12):127204.
85 Kresse G, Hafner J. 1993. Ab initio molecular dynamics for liquid metals. *Phys Rev B*. 47(1):558.
86 Blöchl PE. 1994. Projector augmented-wave method. *Phys Rev B*. 50(24):17953.

87 Monkhorst HJ, Pack JD. 1976. Special points for Brillouin-zone integrations. *Phys Rev B*. 13(12):5188.
88 Togo A, Oba F, Tanaka I. 2008. First-principles calculations of the ferroelastic transition between rutile-type and $CaCl_2$-type SiO_2 at high pressures. *Phys Rev B*. 78(13):134106.
89 He X, Helbig N, Verstraete MJ, Bousquet E. 2021. TB2J: a python package for computing magnetic interaction parameters. *Comput Phys Commun*. 264:107938.
90 Liechtenstein A, Katsnelson MI, Antropov VP, Gubanov VA. 1987. Local spin density functional approach to the theory of exchange interactions in ferromagnetic metals and alloys. *J Magn Magn Mater*. 67(1):65–74.
91 Marzari N, Mostofi AA, Yates JR, Souza I, Vanderbilt D. 2012. Maximally localized Wannier functions: theory and applications. *Rev Mod Phys*. 84(4):1419.
92 Mostofi AA, *et al*. 2014. An updated version of Wannier90: a tool for obtaining maximally-localised Wannier functions. *Comput Phys Commun*. 185(8):2309–2310.
93 Toth S, Lake B. 2015. Linear spin wave theory for single-Q incommensurate magnetic structures. *J Phys: Condens Matter*. 27(16): 166002.